DOUBLE-BLIND REVIEW

Average Q_p and Q_s-estimation in Marine Sediments using a Dense Receiver Array

Running head: Average Q estimation in Marine Sediments

Robin André Rørstadbotnen* and Martin Landrø*

* Norwegian University of Science and Technology, Department of Electronic Systems, NO-7491, Trondheim, Norway

E-mails: robin.a.rorstadbonen@ntnu.no and martin.landro@ntnu.no

Average Q_p and Q_s-estimation in Marine Sediments using a Dense Receiver Array

(October 14, 2022)

Running head: **Average Q estimation in Marine Sediments**

ABSTRACT

A new spectral ratio method has been used to compute average P- and S-wave quality factors, Q_p and Q_s, for the sedimentary sequence below the 'V'-shaped Oseberg Permanent Reservoir Monitoring (PRM) system. Quality factors are important for a more accurate characterization of the subsurface and to get additional information on the physical processes within the earth, such as fluid content and partial melt. However, few methods compute the average Q-value in sediments for both P- and S-waves in a region, which can be used as a constraint for attenuation models in more sophisticated inversion techniques like full-waveform inversion or attenuation tomography. To address this, a spectral ratio method using two receiving stations, one installed on sediment and one installed on bedrock, was developed. This resulted in quality factor estimations ranging from approximately 64 to 137 for P-waves and 29 to 123 for S-waves using a subset of the 172 ocean bottom nodes in the Oseberg PRM system and a seismometer in Bergen, Norway. The Q_p values are more scattered and hence more uncertain than the Q_s values due to the P-wave signal being close to the background noise level. In the study area, local earthquakes of magnitude as low as

3

M_L 2.4 can be used to get Q_p values and earthquakes of magnitude lower than 2.1 to find Q_s values, with the possibility of using lower magnitude events if the epicentral distances to the receivers are similar, and smaller. Using this method, the average quality factor in sediment packages can be estimated using appropriate source and receiver, and hence ray path, configurations for a variety of regions.

INTRODUCTION

Seismic waves are known to attenuate when propagating through the subsurface. This wave attenuation will reduce the amplitude of the signal with increasing propagation distance, leading signals at some frequencies to fall below the noise floor, decreasing the frequency bandwidth. It will also cause a frequency-dependent phase shift, and therefore, a waveform change. The seismic attenuation is often described by the quality factor Q, a measure of the efficiency of wave propagation, or its inverse, Q^{-1}, the internal friction (Stein and Wysession, 2003; Romanowicz and Mitchell, 2007). Q can be specified for different types of waves, as they show different attenuation behaviour when propagating through the same geology. This paper focuses on the average quality factor for P- and S-waves through a given sediment package, Q_p and Q_s. It has also been observed that the quality factor varies for different types of geology. In sedimentary layers, the value is normally much lower than in bedrock. Low Q values mean that the seismic wave amplitudes attenuate more and experience more phase change than high values. In addition, an important consequence of attenuation is physical dispersion, where a high attenuation causes a high dispersion. Conversely, a low attenuation will produce little to no dispersion (Stein and Wysession, 2003). In general, two main mechanisms control the level of attenuation: seismic absorption (heat loss) and scattering. No discrimination between the two will be made; instead, the effective, or combined, attenuation is studied. Attenuation is recognized as a significant seismic parameter which, when known and compensated for, may allow for improved interpretation of seismic data. Furthermore, due to the high variation of Q

values in the crust and uppermost mantle, this parameter can be related to additional geological and geophysical information that can not be found using other geophysical tools. This information can subsequently be used, for example, to more confidently characterize oil and gas reservoirs, monitor CO_2 injection, magnitude estimation of earthquakes, map 3D geological structures and dynamics within the Earth and provide improved estimates of synthetic seismograms (Aki, 1980; Stainsby and Worthington, 1985; Tonn, 1991; White, 1992; Hauksson and Shearer, 2006; de Lorenzo et al., 2013; Amalokwu et al., 2014).

In addition to variation in the crust and the uppermost mantle, the quality factor can be affected by the regional geology, such as differences observed within and at the interface between the crust, mantle, and core (Mitchell, 1995; Romanowicz and Mitchell, 2007). In order to map the crust and mantle attenuation, tomographic analyses have been carried out for the entire Earth. Mitchell et al. (2008) mapped, for example, the overall trend for Eurasia. However, these tomographic models do not capture the local variation of the Q-values, e.g., the difference between the local Q value in sediment packages and bedrock as studied here. Moreover, there are several studies that capture the local attenuation in a given area: Beckwith et al. (2017) used prestack Q inversion for a seismic reflection survey in the North Sea, Zollo and de Lorenzo (2001) used a pulse width method in Flegrei Caldera (Italy) and, more recently, Sketsiou et al. (2021) found a 3D attenuation image of the Pollino fault network in Italy. Other studies on oil and gas fields characterize the attenuation values through analysis of well data (see, e.g., Reid et al. (2001); Sams et al. (1997);

5

Carter et al. (2020)). This work aims to add a new spectral ratio method for local attenuation estimation to these studies. The method was developed to estimate Q values of a sedimentary package for both P- and S-waves using station pairs, one station placed on sediment, and one placed on bedrock using earthquakes as the source. The method provides average estimates of the given sedimentary package that can serve, for example, as a model constraint for more complicated estimation methods, like full-waveform inversion and attenuation tomography. The quality factor for a 5-7 km thick sediment package below Oseberg C has been estimated using a permanent reservoir monitoring (PRM) system and a seismometer in Bergen, Norway (Figure 1). The method has been applied to three local earthquakes recorded in January 2014.

The method presented in this paper contains comparable aspects to the procedure developed by Teng (1968) and later applied by, e.g., Solomon (1973) and Hwang et al. (2009). Furthermore, others have applied spectral ratio to estimate Q values. Dasgupta and Clark (1998) used spectral division on conventional surface seismic common mid-point reflection data to find seismic attenuation values in the southern North Sea. Later, Liu et al. (2018) used a modified log spectral ratio method to find Q values, and Mayeda et al. (2007) used a coda spectral ratio of narrowband envelopes to find the attenuation. Hauge (1981) measured attenuation from vertical seismic profiles using spectral ratios between downhole pulses and a reference pulse. The proposed method differ from the listed ones by taking the spectral ratio of a station pair, with one receiver located on sediment and the other on bedrock, to estimate the

6

quality factor value of a sedimentary sequence for both P- and S-waves.

DATA AND THEORY

Earthquakes recorded on receivers at the Oseberg field, the North Sea, and Bergen, Norway (Figure 1) were analyzed in this work. The Oseberg data (OSE) were acquired on 172 4-component (C) ocean bottom nodes (OBN) connected by a seismic cable, containing 3-orthogonal geophones and one hydrophone, as part of the 'V' shaped Oseberg PRM system. The sensor spacing of the outer legs are 50 m and 25 m on the inner legs (see Figure 1C) and trenched 1-2 m into the seabed at a water depth of 108 m (Bussat et al., 2016). The data recorded in Bergen (BER) were recorded on a 3-C broadband seismometer located at the University of Bergen campus. Only one month of data from the Oseberg PRM was available for the analysis (2014.01), three local earthquakes were visible in the data and hence focused on in this analysis. These events will be denoted as E1 for the earthquake on 2014.01.14, E2 for the earthquake on 2014.01.21 and E3 for the earthquake on 2021.01.23. Key facts about the earthquakes are summarized in Table 1. Note that no depth estimate was provided for the low magnitude E1 due to its remote location and distance to the receivers. In addition, six teleseismic earthquakes were reported by USGS (2022) with magnitudes higher than M_{ww} 6.1, with a maximum magnitude of 6.5. There were two main reasons why these were not included in the analysis: (1) as the method estimates the quality factor of the sedimentary layer at the end of the wave propagation path, the teleseismic signal will be dominated by the signal propagating in the bedrock and

mantle, and hence not focusing on the effects occurring in the sedimentary layer. (2) The magnitudes of the events were relatively small with a long propagation path (the smallest propagation distance is 2700 km with a magnitude of 6.1).

Pre-processing

In order to prepare the Oseberg PRM data for Q-value estimation, various pre-processing steps were carried out. (1) Platform noise present in the Oseberg data was suppressed using an fx-filter (Schonewille et al., 2008). The noise was suppressed by four iterations using a noise threshold of seven with five filter points and a frequency band from 1 to 50 Hz (Figure 2). An example of the data from E3, and the effect of the platform noise removal, can be seen in Figure 2. The fx-filter only changes the noise portions of the data, leaving the earthquake signal (and therefore the spectrum) untouched (Schonewille et al., 2008). This can also be observed in the difference plot in Figure 2C, where only the noise part has been affected while the earthquake signal was not. (2) The Oseberg data were converted from g (using a constant factor of 9.81 m/s^2) to particle acceleration and further integrated to particle velocity to match the same measurement unit as the BER seismometer. (3) The data were de-trended, and (4) all the data were resampled to a common sample rate. Since only frequencies from the local earthquakes were of interest, (5) a Tukey window and a 4th order Butterworth band-pass filtered with cut-off frequencies at 1 and 40 Hz were applied. The low-cut frequency was set to 1 Hz to remove the most prevalent part of the ocean noise at Oseberg.

Travel-time computation

A ray tracing algorithm was used to compute the travel times needed in the analysis. To calculate these values, a P-wave velocity model representing the geology in the Oseberg area was constructed. This velocity model was generated using the same approach as Jerkins et al. (2020) by combining a local sonic log from well 30/6-1 (Figure 3A), and a regional layered velocity model of the area (Havshov and Bungum, 1987), as shown in Figure 3(A-B). The ray tracing algorithm is a high-frequency approximation to the wave equation and therefore requires a smooth velocity model as input (Figure 3C). The smoothing ensures that the characteristic dimensions of inhomogeneities were considerably larger than the prevailing wavelength in the model (Cervenỳ, 2001). Hence, a four-step workflow to find a smoothed representation of the combined velocity model was employed. (1) The rapid changes in the sonic log were smoothed as shown in Figure 3A using a 0.76 km moving average window. (2) The end of the sonic log ($\simeq$3.2 km depth) was connected to the regional velocity model at 8.125 km depth (Figure 3B). (3) Linear interpolation was applied so that the entire model had the same depth sampling interval. Finally, (4) a moving-average filter with a window of 3.048 km was applied for the final smoothing. The linear interpolation and moving average filter were chosen for simplicity and efficiently smoothed the data to the wanted level.

The ray tracing algorithm used to model the ray paths through the subsurface was based on the ray equations. The ray equations are used to approximate the non-linear

eikonal equations and given by (Thomson and Chapman, 1985; Keers et al., 1997):

$$\frac{d\mathbf{x}}{dt} = v^2(\mathbf{x})\mathbf{p}, \tag{1}$$

$$\frac{d\mathbf{p}}{dt} = -\frac{1}{v(\mathbf{x})}\nabla v(\mathbf{x}) \tag{2}$$

The modified Euler method was used to numerically implement the equations:

$$\mathbf{x}_{i+1} = \mathbf{x}_i + \Delta t v^2(\mathbf{x}_i)\mathbf{p}_i, \tag{3}$$

$$\mathbf{p}_{i+1} = \mathbf{p}_i - \Delta t \left(\frac{1}{v(\mathbf{x}_{i+1})} \frac{\partial v(\mathbf{x}_{i+1})}{\partial \mathbf{x}} \right) \tag{4}$$

where $\mathbf{x}$ is the position along the ray, $v(\mathbf{x})$ is the velocity from the velocity model, Δt is the time step and $\mathbf{p}$ the slowness vector.

Q-estimation using spectral division of data from two sensors

In order to estimate the Q-value for the sediment package underneath the Oseberg C platform, a spectral division method was applied to the signals recorded on the Oseberg PRM system and the BER seismometer. Note that the quality factor was assumed to be frequency independent. This is a common, but questionable, assumption as discussed by Douglas (1992); Sams et al. (1997); Romanowicz and Mitchell (2007); Beckwith et al. (2017), among others. As depicted in Figure 3C, the ray paths to OSE propagate through a layered bedrock model at the start and later through a 5-7 km thick sediment layer before being recorded. In contrast, the ray paths to BER travel primarily through the layered bedrock model. The layered bedrock model was created based on previous studies from the North Sea (Dasgupta and Clark, 1998; Reid et al., 2001; Mitchell et al., 2008). Following these definitions, the predicted

10

amplitudes recorded at OSE (A_1) and BER (A_2) can be given, under the low-loss condition ($Q \gg 1$), as (Stein and Wysession, 2003):

$$A_1 = \frac{S}{R_1} \exp\left(-\pi f \frac{T'_{sed}}{Q_{sed}}\right) \exp\left(-\pi f \sum_{i=1}^{N_1} \frac{T'_i}{Q_i}\right), \tag{5}$$

$$A_2 = \frac{S}{R_2} \exp\left(-\pi f \sum_{k=1}^{N_2} \frac{T_k}{Q_k}\right) \tag{6}$$

where S is the source signature, T'_{sed}, T'_i, and T_k are the travel time through the sedimentary layer, through layer i to the sediment package and through layer k to BER, respectively. N_1 and N_2 are the numbers of bedrock layers the ray travel through. R_1 and R_2 denote the geometric spreading factors and are given as the travel distances to OSE and BER, respectively. Q_{sed} represents the average attenuation in the sediment package. Q_i and Q_k are the attenuations in the bedrock layers.

By performing a spectral division between the predicted amplitude at OSE with that of BER, the following expression was obtained:

$$\frac{A_1}{A_2} = \frac{R_2}{R_1} \frac{\exp\left(-\pi f \frac{T'_{sed}}{Q_{sed}}\right) \exp\left(-\pi f \sum_{i=1}^{N_1} \frac{T'_i}{Q_i}\right)}{\exp\left(-\pi f \sum_{k=1}^{N_2} \frac{T_k}{Q_k}\right)} \tag{7}$$

which can be rewritten into the following form:

$$\ln\left(\frac{A_1}{A_2}\right) = \ln\left(\frac{R_2}{R_1}\right) - \pi f \left(\frac{T'_{sed}}{Q_{sed}} + \sum_{i=1}^{N_1} \frac{T'_i}{Q_i} - \sum_{k=1}^{N_2} \frac{T_k}{Q_k}\right) \tag{8}$$

from this, the coefficients of a straight line with slope a and intercept b can be defined:

$$b = \ln\left(\frac{R_2}{R_1}\right), \tag{9}$$

$$a = -\pi \left(\frac{T'_{sed}}{Q_{sed}} + \sum_{i=1}^{N_1} \frac{T'_i}{Q_i} - \sum_{k=1}^{N_2} \frac{T_k}{Q_k}\right) \tag{10}$$

Subsequently, the slope can be found by linear regression of the ratio $\ln(A_1/A_2)$ for a frequency range above the noise floor for both signals. Rearranging, the average

quality factor in the sediment package, Q_{sed}, can be computed using the measured slope:

$$Q_{sed} = \frac{T'_{sed}}{-\frac{a}{\pi} - \sum_{i=1}^{N_1} \frac{T'_i}{Q_i} + \sum_{k=1}^{N_2} \frac{T_k}{Q_k}} \tag{11}$$

Note that the spectral ratio eliminates the effects of the source term, while geometrical spreading is accounted for in the intercept b, independent from the final Q_{sed} estimation. Furthermore, the effect of instrument response on the recorded earthquakes is expected to be the same for all the receivers, since the dominant frequency range is within the flat part of the instrument response for both receiver types used. Common values for the different terms are summarized in Table 2, where the notation has been simplified by letting $t^* = \sum t/Q$ and hence:

$$\Delta t^* = -\sum_{i=1}^{N_1} \frac{T'_i}{Q_i} + \sum_{k=1}^{N_2} \frac{T_k}{Q_k}. \tag{12}$$

Uncertainty analysis

The quality factor given in equation 11 is a function of the slope, a, the travel time through the sediment layer, T'_{sed}, and the travel time differences divided by the assumed quality factor in the bedrock, Δt^*. By assuming that the parameters, a, T'_{sed}, Δt^*, are independent of each other, an estimation of the uncertainty related to Q_{sed} can be found through:

$$\delta Q_{sed} = \sqrt{\left(\frac{\partial Q_{sed}}{\partial a} \delta a\right)^2 + \left(\frac{\partial Q_{sed}}{\partial T'_{sed}} \delta T'_{sed}\right)^2 + \left(\frac{\partial Q_{sed}}{\partial \Delta t^*} \delta \Delta t^*\right)^2} \tag{13}$$

where δa is the standard error of the slope found in the regression analysis, $\delta T'_{sed}$ and $\delta \Delta t^*$ are, in this case, errors related to an erroneous velocity model used to compute

12

the travel times through the sedimentary sequence and the bedrock. The errors in the velocity model are assumed to be 15%, based on the variation in the sonic log from well 30/6-1 (see Figure 3A). Moreover, the weak point of this method, in this scenario, is that the parameters, T'_{sed} and Δt^*, are not fully independent. Therefore, the assumption is that they are weakly related to each other and can thus be treated as independent (Landrø, 2002). Furthermore, the uncertainty parts in equation 13 are assumed independent, i.e., that they are orthogonal and, hence, a conservative estimate of the total uncertainty of Q_{sed}. The partial derivatives in equation 13 are given as:

$$\frac{\partial Q_{sed}}{\partial a} = \frac{T'_{sed}}{\pi \left(\frac{-a}{\pi} + \Delta t^* \right)^2} \tag{14}$$

$$\frac{\partial Q_{sed}}{\partial T'_{sed}} = \frac{1}{\frac{-a}{\pi} + \Delta t^*} \tag{15}$$

$$\frac{\partial Q_{sed}}{\partial \Delta t^*} = \frac{-T'_{sed}}{\left(\frac{-a}{\pi} + \Delta t^* \right)^2} \tag{16}$$

and, hence, the uncertainty in the average quality factor as:

$$\delta Q_{sed} = \sqrt{ \left(\frac{T'_{sed} \cdot \delta a}{\pi \left(\frac{-a}{\pi} + \Delta t^* \right)^2} \right)^2 + \left(\frac{\delta T'_{sed}}{\frac{-a}{\pi} + \Delta t^*} \right)^2 + \left(\frac{-T'_{sed} \cdot \delta \Delta t^*}{\left(\frac{-a}{\pi} + \Delta t^* \right)^2} \right)^2 } \tag{17}$$

RESULTS AND DISCUSSION

The Q-estimation

The Q_{sed} values are computed using a subset of the 172 receivers available at Oseberg. The stations closest to the platform (channels 1-14 and 158-172 inclusive) are visibly highly contaminated by platform noise and are a priori discarded from the analysis.

To find reliable channels, two conditions based on signal-to-noise ratios (SNR) are introduced (see Appendix A for computation of SNR).

The first SNR condition uses the root-mean-square (RMS) of equal length windows to compute the SNR. The three windows are: (1) before the P-wave arrival assumed to only contain noise (noise RMS), (2) after the P-wave arrival, including the P-wave signal (P-wave RMS) and (3) after the S-wave arrival including the S-wave signal (S-wave RMS). Figures 4(A,B,E,F) show examples of how the first-breaks are found on the OSE and BER data (see Appendix B for a comparison between high and low SNR waveforms from OSE). The window length is defined as the time interval between the P- and S-wave arrivals for the sensor closest to the event investigated, i.e., the station with the shortest P-S delay. From the resulting RMS values shown in Figure 5(A,C,D) it is possible to see the differences in signal quality for receivers in different portions of the PRM system. Channels at distances 3.08-3.58 km (channel number 80-100) are observed to have the highest RMS level for the received P- and S-waves for both E2 and E3, perhaps due to better sensor coupling. Comparing the RMS noise from the window just before the P-wave signals to RMS from 3 hours of data, assumed to contain noise only, the noise before E2 is lower than the mean for the 3 hours of data, while the noise for E3 is similar (see Figure S1 in supplemental material for mean noise RMS). The lower noise RMS for E2 is most likely due to the platform noise suppression being more efficient for this event compared to E3. The noise level for E2 is on average 0.71 μm/s compared to 0.98 μm/s for E3. The SNR level at which the estimated quality factor becomes stable (7.5 dB for P-arrivals, all S-wave arrivals) is

then chosen, and channels with SNR above these boundaries are considered reliable. Figure 5 shows the computed RMS values (A,C,E) and the associated SNR values and boundary (B,D,F). As expected, E3 shows the highest RMS and SNR values for the S-wave and E1 the lowest. It is also evident that the P-wave arrives with low amplitudes, barely above the noise floor for all earthquakes. By investigating the frequency content of the noise, P-, and S-wave signals in Figure 4(C-D), clear differences are observed. The BER amplitude spectrum exhibits more high-frequency components than the OSE amplitude spectra. This is interpreted to be due to the extra attenuation caused by the sediment package under the Oseberg PRM system as schematically illustrated in Figure 3C. Furthermore, the noise level at OSE is higher than BER, especially for low frequencies, even after suppressing the platform noise and ocean swell noise in the pre-processing. This is expected because the OBN network is affected by more low-frequency swell noise than the on-land BER seismometer.

The second condition compares the frequency component of the noise to the P- and S-wave frequency spectra, and the SNR for all components are calculated. Only channels with high enough SNR to adhere to condition one are considered. In order to estimate reliable slopes from the spectral division, high SNR for as many frequency components as possible is needed. The SNR boundary for both waves is set to 10 dB. The frequency SNR boundary is displayed in Figures 6(G-H) together with the spectral ratio for P- and S-wave obtained by taking the ratio between the smoothed amplitude spectra of a station pair depicted in Figures 6(A, B, D, E). The smoothing is carried out to remove the effects of the frequency component close to

zero, resulting in unstable division and a large effect on the final results. The effects of the frequency components close to zero are especially problematic for the higher frequencies as can be observed in Figure 6(C, F, I). The bold portion of the spectral ratio in Figure 6 indicates the frequencies used in the robust regression (MATLAB's 'robustfit' function was used (Dumouchel and O'Brien, 1989)) to estimate the slope and the associated uncertainties, a and δa, respectively (for more examples see Figures S2 to S7). The slopes with a 95% confidence interval and the associated standard residual error (SRE) are represented in Figure 7(A-B).

The estimated travel times through the sedimentary layer, T'_{sed}, and the difference in t^* values from the travel time in the layered bedrock model, Δt^*, for all earthquakes analyzed are depicted in Figure 8 (see Figure S8 in supplemental material for examples of computed ray paths used to find these values).

Applying the values from the ray tracing, the SNR conditions and the obtained slopes, the Q_{sed} values are estimated for both the P- and S-wave arrivals. The attenuation results are plotted together in Figure 7C and individually along the array lay-out in Figure 9. In order to find the best boundaries for the first SNR condition, a plot without the introduced SNR boundary is made for comparison (see Figure 10). By comparing the estimates and the uncertainty found in equation 17 with and without the boundary (Figure 7C vs Figure 10) and the associated SNR for each channel (Figure 5) it is clear that the P-wave attenuation values become unstable under approximately 7.5 dB, while the Q_s values are stable for all channels. For the Q_p values, the total uncertainty is generally high for the rejected values. However, some values

have uncertainty close to the accepted values (e.g., the E1 estimates). These were considered unstable due to their low SNR, where their first-break arrivals were hardly visible in the waveforms. From this, a 7.5 dB boundary is set for the Q_p estimation, and no boundary for Q_s is set. This condition provides 27 estimated Q_p values and 378 estimated Q_s values for the events. Note that the estimated quality factor values are given as the mean and one standard deviation from the estimates obtained (see Table 2). The values for the quality factor and the associated uncertainties (from equation 17) are given separately.

The results will be presented and discussed in four parts, starting with discussing the effects of the assumed values, followed by a presentation and discussion of the results based on the epicentre location, starting with E1, then E2 and E3. Finally, a comparison of the results will be presented.

Assumptions affecting the results

The model for the bedrock attenuation Q and the constant parameter for the sediment thickness used in the estimation are assumed to be known. These are based on results from previous Q and geological studies of the North Sea. Mitchell et al. (2008) used attenuation tomography to estimate Q_{Lg} values for the entire Eurasia plate and found the quality factor value to be $\simeq 900$, i.e., a non-attenuating media, for the Oseberg area. Whereas Dasgupta and Clark (1998) and Reid et al. (2001) found local quality factor values to be between 81 and 1000 for sedimentary and bedrock in the North Sea. Furthermore, Beckwith et al. (2017) found a quality factor between 161 and

182 over the Kinnoull oil and gas field. These studies provide the area's widest range of credible values, and a three-layered Q model was chosen based on them (see Figure 3C). Furthermore, the exact thickness of the sediment package varies due to the Oseberg mega-block and ranges typically from 5 to 7 km (Færseth and Ravnås, 1998). This induces uncertainty in the estimated Q_{sed} values as the computed travel times in the sedimentary sequence depend on the thickness. Decreasing the thickness of the sediment layer will decrease the travel time value in the sedimentary layer (T'_{sed}) and increase the travel time in the bedrock (T'). The consequence is that the Q_{sed} value will decrease as the decrease in T'_{sed} has a bigger effect on the quality factor estimate than the increase in T'. Decreasing the thickness of the sedimentary layer from 7 km to 5 km gives an average quality factor decrease of 18 for the events studied. The results presented in Figure 7C are found using a sediment layer thickness of 7 km.

A one-dimensional velocity model for the oceanic crust is used to estimate the travel time values. As mentioned in the theory section, it is created by combining a well near Oseberg (30/6-1) with a regional velocity model. The model provides reliable travel time values for the ray paths close to the Oseberg PRM system, as the rays are propagating through geology captured by the sonic log used to create the velocity model. It will, however, not provide the same accuracy for the ray paths to BER as the station is located on the continental crust. The rays to BER travel either through continental crust only (E2 and E3) or through a combination of oceanic and continental crust (E1). This introduces uncertainties to travel times, especially for

rays propagating in the continental crust. Nevertheless, using a 1D model provides sufficient accuracy to the travel times to show the reliability of this method. Further investigation into the effect ray tracing using a 3D velocity model capturing all, or some, of the heterogeneity in the area, including the effect of the Oseberg mega-block and the differences in seismic velocities between oceanic and continental crust, has on the quality factor estimation is outside the scope of this paper.

It is assumed that the source signature is cancelled in the spectral division in equation 7. However, earthquakes are not isotropic sources. The effect of the source will be cancelled when the stations are in the same azimuth direction from the earthquakes. For the event in this study, the azimuth differences are 33°, 93° and 78° for E1, E2 and E3, respectively, which means that the source signature will not be the same and not entirely cancelled out in the spectral ratios.

Notches due to free-surface multiples are observed in both the hydrophone and geophone data. For the geophone data, four notches are observed at 3.5, 10.4, 17.4, and 24.4 Hz within the earthquake signal bandwidth, while the notches in the hydrophone recordings are found at 0, 7.0, 13.9, 20.9 Hz. Note that the notch at 0 Hz is a combination of the first free-surface multiple-related notch and that the hydrophone instrument response is close to 0 Hz at this frequency. These notches agree with the modelled first-order free-surface multiple notches for a 107 m water depth (see Appendix C). However, compensating for their effect did not affect the estimated attenuation values and was not included in the workflow but should be considered when estimating the sediment quality factor from similar OBN data.

Results E1

The epicentre of the earthquake recorded 2014.01.16 was found to be 142 km and 239 km south-east of the Oseberg PRM system and the BER seismometer, respectively (Figure 1). This M_L 2.11 earthquake is the lowest magnitude event used in this study, also reflected in the computed RMS and SNR values (Figure 5). From the SNR and the clarity of first-break P- and S-phase arrivals, the ranges of the a priori omitted channels were increased to 1-27, 73-100, and 144-172. Furthermore, due to the event's low magnitude and remote location, NNSN and NORSAR did not obtain a reliable depth estimation. A depth of 11 km, similar to the other events, was assumed for the earthquake. From the error ellipse presented in NORSAR's seismic bulletin (NORSAR, 1971), the location of the earthquake was observed to contain significant uncertainty (Figure 1). Since the sediment attenuation estimates rely on modelled travel times from the event to the receivers, accurate hypocenter information is important, and uncertainty in the location induces uncertainty in the Q_{sed} estimation. Moreover, the travel path from E1 to OSE and BER is primarily through the oceanic crust, with varying distances. From the ray tracing, the average travel time differences are found to be $\simeq$34.7 s for the S-wave arrivals. Another effect of the long travel distance is that the seismic waves dive deeper into the subsurface and encounter the sediment package at higher angles (relative to the horizontal axis), decreasing the travel times in the sedimentary sequence. Using the travel times, slopes, and assumed values, 89 Q_{sed} values adhered to the first SNR condition and were estimated with a mean and one standard deviation of 50 ± 6, where the standard

deviation represents the spread in the estimated values. The low estimated quality factor and low variability over the different estimates are due to the big travel time difference systematically decreasing the final estimates; this will be discussed in more detail in the 'Comparison' section. Moreover, the average total uncertainty related to the estimates was found to be 8.7 over the estimated values using equation 17. The individual Q_{sed} estimates, with related uncertainty, are shown in Figure 7C.

Results E2 and E3

The second (M_L 2.35) and third (M_L 2.57) earthquakes recorded on 2014.01.22 and 2014.01.23 had epicentres $\simeq$88 and $\simeq$107 km north-east of OSE, respectively, and $\simeq$107 and $\simeq$119 km north-west of BER. These events have also uncertainties related to their hypocenter estimates inducing uncertainty in the computed travel times (Figure 1). Moreover, the seismic waves generated by the earthquakes travel through different geology to OSE and BER. The propagation to OSE is mainly through the oceanic crust, while it propagates through the continental crust to BER. The travel times to the receivers are similar, with an average P-wave travel time difference of $\simeq$0.8 s for both E2 and E3. The average S-wave travel time differences are $\simeq$1.45 s. Furthermore, due to the shorter travel distance (compared to E1), the rays will not dive as deep into the subsurface; hence encountering the sediment package at a lower angle increases the travel times in the sediment package (Table 2).

Figure 7C displays the 26 P-wave attenuation values and 145 S-wave attenuation values estimated for E2, with values ranging from 64 to 137 and from 60 to 123,

respectively. In the same plot, the single estimated P-wave value and the 144 S-wave attenuation values for E3 are shown. The Q_p value for E3 is 65, while the Q_s values range from 60 to 121, resulting in an average Q_s estimation with one standard deviation of 93 ± 13 over the estimated values. The related mean uncertainties for Q_p and Q_s are, respectively, 10.3 and 14.7, as computed from equation 17. Furthermore, the Q_p and Q_s average estimates for E2 are 92 ± 19 and 85 ± 13, with average uncertainties of 14.2 and 13.3. It is also possible to compute the Q_s/Q_p value for E2 by taking the ratio between values obtained from corresponding channels. Using the central channels at distances 3.0-3.58 km (channels 77-100, excluding channels 78 and 98 due to low SNR), a ratio of 0.9 ± 0.2 is found. Similarly, the ratio between the single Q_p value for E3 and the corresponding Q_s is 1.4. However, we will not put any emphasis on this value due to it being obtained by only one data-point. The ratio found for E2 is considered more reliable due to it being estimated from 22 data-points. Table 3 summarises the estimated values.

Comparison

There are obvious differences between the travel path from E1 and E2-E3. (1) The travel distances from E1 to the receivers are longer than for E2 and E3. (2) The travel time differences are larger for E1. (3) The seismic waves propagate through different media. The travel distances only change the depths the rays reach, and hence the travel time in the sediment layer (T'_{sed}). From the ray tracing, the estimated S-wave travel times in the sedimentary sequence decrease $\simeq 11.8\%$ from E1 to E2 and E3.

Moreover, when a large travel time difference is present in the Δt^* term of equation 11, it will influence the Q_{sed} estimates. For E1, this term is the same as the average slope term value $(-a/\pi)$, with the same sign, which creates a systematic decrease in the attenuation estimation of the sediment package (see Table 2). Comparing E1 to E2 and E3, these terms are only $\simeq 14\%$ and $\simeq 23\%$ of the obtained average slope term values, respectively. Hence, the hypocenter position relative to the receiver pair will affect the end estimates of the attenuation value. If the travel time difference term is neglected, and only the average slope values are considered, the estimates would be similar for the three events. From the slope values listed in Table 2 and depicted in Figure 7A the Q_{sed} values of E1 would be estimated around the E2 and E3 values. Therefore, a too large travel time difference might introduce a systematic error in the method, whereas more reliable values are obtained when the difference is low. However, this depends on the accuracy of the assumed bedrock Q model. The dependence on the bedrock Q model can be avoided by choosing the receiver pair and the earthquake carefully. The emerging distributed acoustic sensing technology will increase the station coverage both on land and in the ocean worldwide (Lindsey et al., 2017; Williams et al., 2019), and choosing a station pair that optimizes the estimation procedure will be easier.

From Figure 9 the Q_{sed} values are plotted for the array lay-out. The values for Q_s for all events show a frequency-dependent array response, especially clear for E2, where the segment oriented in the north-south direction shows an all-over lower Q value than the east-west oriented segments. Moreover, looking only at the quality

factor values for the north-south oriented segment, the standard deviation of the Q_s estimates over the array decreases to 5.4 (E1), 8.8 (E2) and 9.7 (E3), a decrease of, respectively, 0.9, 4.1 and 0.9. The Fresnel zones of the events are, on average, 6.2 km (E1), 5.3 km (E2), and 5.6 km (E3), which is considerably larger than the maximum array aperture of 1.75 km. From these Fresnel zones, there should not be large variations along the array. The exact nature of the response along the array is not known and is beyond the scope of the work in this paper. However, the fact that amplitudes along various branches of the array are aligned points toward a frequency-dependent array-effect caused by the cable orientation. Another possible explanation for the variation can be near-surface effects. These effects can affect the observed amplitudes on the array. Malme et al. (2005) investigated the effects of overburden diffractors and shallow lenses and found that they lead to considerable local amplitude variation. The diffraction led to rapid oscillation in the amplitude level observed, while the lenses distort reflection events. Near-surface effects like these have not been studied in the current work.

From the robust regression algorithm used the 95% confidence interval (Figure 7A) and the standard residual error (SRE, Figure 7B) are estimated for the three earth-quakes. The latter show similar values over all earthquakes, where the lowest average SRE is related to E1 (0.023 s), the highest to E2 (0.030 s), and E3 between the two (0.027 s). The lower SRE value for E1 is related to the lower portion of the frequency spectra used in the regression analysis, which behaviour is better represented by a linear regression line (see, for example, Figures S2, S3 for E1, Figure S4 for E2 and

24

Figures S5, S6, S7 for E3 in supplemental material). Furthermore, using equation 17 the uncertainty as a function of the different variables in equation 11 are found. Figure 11 and Figure 12 show the total uncertainty in Q_p and Q_s, respectively, for E2, as a function of the different variables (see Figure S9 for equivalent plots for E1 and Figures S10, S11 for E3 in supplementary material). By varying the slope, a, a strong dependence is observed, where an increase in the slope value is related to a higher uncertainty while a decrease a lower uncertainty. By increasing T'_{sed}, the uncertainty will also increase. Conversely, the uncertainty related to Δt^* will decrease when its value increases. Furthermore, a decrease in the velocity model is related to a higher uncertainty than an increase in the velocity model.

The estimated Q_p and Q_s-values found in this work agree with previously published values for sedimentary successions, including values estimated from North Sea deposits. Sheriff and Geldart (1995) mapped general Q_p values for different rock types, and found the value to range from 20-200 for sediments. Others have found attenuation values in sediments between 20-200 for the North-Sea (Kang and McMechan, 1994; Dasgupta and Clark, 1998; Reid et al., 2001; Allmark et al., 2018; Carter et al., 2020), providing the widest range of credible values. From the three earthquakes recorded in January 2014, values ranging from 64 to 137 for P-waves and 29 to 123 for S-waves were found, with an average total uncertainty of 14.0 and 12.7, respectively. E2 and E3 show similar values, which is expected for seismic waves propagating through similar geology.

CONCLUSION

We developed a new method that estimates average quality factors for a given sedimentary package for recorded P- and S-wave, Q_p and Q_s, using the spectral ratio for a station pair, one located on sediment and one on bedrock. Exploiting three earthquakes (E1, E2 and E3) recorded on 172 seabed receivers in the Oseberg PRM (Permanent Reservoir Monitoring) system and a seismometer in Bergen, a total of 27 Q_p and 378 Q_s values were estimated for the sediment package under the PRM system at Oseberg. The mean estimated Q_p values are 92 ± 18, where the confidence interval represents the spread in the estimated values. Furthermore, similar Q_s values were found for E2 and E3, respectively, 84 ± 13 and 93 ± 13. Moreover, the average uncertainty for the Q_p and Q_s estimates over the array were found to be 14.0 for both. Estimated Q_p and Q_s values from E2 give a Q_s/Q_p of 0.9 ± 0.2, while E3 estimates gives a Q_s/Q_p of 1.4. The estimated P-attenuation value for E2 is the most reliable value because of more estimated values for E2 (22) than E3 (1). The ratio suggests a bigger attenuation for S-waves than P-waves in this sedimentary layer.

ACKNOWLEDGMENTS

27

APPENDIX A

SIGNAL-TO-NOISE RATIO

The signal-to-noise ratio (SNR) for the P-wave and S-wave signals were computed by:

$$SNR = 20 \cdot \log_{10} \left(\frac{u_{signal}}{u_{noise}} \right) \tag{A-1}$$

where u_{signal} denotes the root-mean-square (RMS) of the P-wave or S-wave signals, and u_{noise} denotes the RMS of a part of the signal assumed to only contain noise. The RMS is given by:

$$u_{RMS} = \sqrt{\frac{1}{N} \sum_{i=1}^{N} u_i^2} \tag{A-2}$$

The second SNR condition, for each frequency component, were computed by

$$U_k = 20 \cdot \log_{10} \left(\frac{|U_{k,signal}|}{|U_{k,noise}|} \right) \tag{A-3}$$

where U_k denotes component k of the frequency domain representation of the signal $(u \leftrightarrow U)$.

APPENDIX B

OBSERVED SIGNALS AND ARRIVAL TIME PICKS

In order to compute the spectral division, we need the arrival times for P- and S-waves. This was done visually by one observer, looking for both a sudden amplitude and frequency change in the data corresponding to the onset of the P- and S-wave.

There are many automatic picking algorithms that can be used to extract this information from the signal and decrease the observer's subjective bias at the cost of other potential limitations in the applied algorithms. For example, the phase detector algorithm developed by Earle and Shearer (1994), the phase picker by Baer and Kradolfer (1987), the artificial neural network approach for P- and S-phase by Gentili and Michelini (2006), or the automatic P-phase picker by Kalkan (2016). The P-wave arrivals were picked using both the vertical geophone and the hydrophone component. The vertical geophone component was, in general, noisier than the hydrophone component (see Figure B-1), and a visual comparison between the two gave a more certain pick of the first break. On the other hand, the S-wave arrivals have a relatively high SNR for all earthquakes for the geophone data, hardly visible in the hydrophone data, and a total of 378 S-wave arrivals were picked using the horizontal components, using the (E-W) component mainly.

APPENDIX C

FREE-SURFACE MULTIPLE RELATED NOTCHES IN THE DATA

In the Oseberg PRM data, we observe notches due to free-surface multiples (see Figure C-1). The water depth at Oseberg has been measured to be $d \simeq 107$ m and the sound speed in water (v) is assumed to be 1480 m/s. We can model the first order free-surface notches in the received signal for both the hydrophone $(G_H(\omega))$ and the

geophone $(G_G(\omega))$ component:

$$|G_H(\omega)| = \left|1 - c_0 \exp\left(i\omega\frac{2d\cos(\theta)}{v}\right)\right| \tag{C-1}$$

$$|G_G(\omega)| = \left|1 + c_0 \exp\left(i\omega\frac{2d\cos(\theta)}{v}\right)\right| \tag{C-2}$$

c_0 is the reflection coefficients of the sea-surface and θ is the offset angle the ray enters the sea column with, measured from the vertical.

We can define the observed amplitude spectrum at OSE, $|P(\omega)|$, as:

$$|P(\omega)|^2 = |S(\omega)|^2|H(\omega)|^2, \tag{C-3}$$

where $|S(\omega)|$ is the received amplitude spectrum unaffected by multiples, $|H(\omega)|^2 = |G(\omega)G(\omega)^*|$ is the predicted ghost power spectrum, and $*$ denotes the complex conjugate. To remove the ghosts in the Oseberg PRM data we rearrange equation C-3 to a spectral division and add a constant factor (η) to avoid division by 0:

$$|S(\omega)| = \sqrt{\frac{|P(\omega)|^2}{|H(\omega)|^2 + \eta}} \tag{C-4}$$

Figure C-1 shows the predicted multiples plotted together with the original amplitude spectrum (black) for the geophone (A, B), the hydrophone recording (C), and the smoothed (30 sample moving average) version (red). A clear correlation between the notches from the data and the predicted interference pattern using the water depth at Oseberg is observed.

REFERENCES

Aki, K., 1980, Attenuation of shear-waves in the lithosphere for frequencies from 0.05 to 25 hz: Physics of the Earth and Planetary Interiors, **21**, 50–60.

Allmark, C., A. Curtis, E. Galetti, and S. de Ridder, 2018, Seismic attenuation from ambient noise across the North Sea Ekofisk permanent array: Journal of Geophysical Research: Solid Earth, **123**, 8691–8710.

Amalokwu, K., A. I. Best, J. Sothcott, M. Chapman, T. Minshull, and X.-Y. Li, 2014, Water saturation effects on elastic wave attenuation in porous rocks with aligned fractures: Geophysical Journal International, **197**, 943–947.

Baer, M., and U. Kradolfer, 1987, An automatic phase picker for local and teleseismic events: Bulletin of the Seismological Society of America, **77**, 1437–1445.

Beckwith, J., R. Clark, and L. Hodgson, 2017, Estimating frequency-dependent attenuation quality factor values from prestack surface seismic data: Geophysics, **82**, O11–O22.

Bussat, S., L. Bjerrum, B. Dando, E. Bergfjord, K. Iranpour, and V. Oye, 2016, Offshore injection and overburden surveillance using real-time passive seismic: First Break, **34**.

Carter, A. J., V. A. Torres Caceres, K. Duffaut, and A. Stovas, 2020, Velocity-attenuation model from check-shot drift trends in North Sea well data: Geophysics, **85**, D65–D74.

Cervenỳ, V., 2001, Seismic ray theory: Cambridge university press, **110**.

Dasgupta, R., and R. A. Clark, 1998, Estimation of Q from surface seismic reflection

data: Geophysics, **63**, 2120–2128.

de Lorenzo, S., E. Del Pezzo, and F. Bianco, 2013, Qc, qβ, qi and qs attenuation parameters in the umbria–marche (italy) region: Physics of the Earth and Planetary Interiors, **218**, 19–30.

Douglas, A., 1992, Q for short-period P-waves: is it frequency dependent?: Geophysical journal international, **108**, 110–124.

Dumouchel, W., and F. O'Brien, 1989, Integrating a robust option into a multiple regression computing environment: Computer science and statistics: Proceedings of the 21st symposium on the interface, American Statistical Association Alexandria, 297–302.

Earle, P. S., and P. M. Shearer, 1994, Characterization of global seismograms using an automatic-picking algorithm: Bulletin of the Seismological Society of America, **84**, 366–376.

Færseth, R., and R. Ravnås, 1998, Evolution of the Oseberg fault-block in context of the northern North Sea structural framework: Marine and Petroleum Geology, **15**, 467–490.

GEBCO, C. G., 2021, Gebco 2021 grid.

Gentili, S., and A. Michelini, 2006, Automatic picking of P and S phases using a neural tree: Journal of Seismology, **10**, 39–63.

Hauge, P. S., 1981, Measurements of attenuation from vertical seismic profiles: Geophysics, **46**, 1548–1558.

Hauksson, E., and P. M. Shearer, 2006, Attenuation models (Qp and Qs) in three dimensions of the southern California crust: Inferred fluid saturation at seismogenic

depths: Journal of Geophysical Research: Solid Earth, **111**.

Havshov, J., and H. Bungum, 1987, Source parameters for earthquakes in the northern North Sea: Norsk Geologisk Tidsskrift, **67**, 51–58.

Hwang, Y. K., J. Ritsema, and S. Goes, 2009, Spatial variations of p wave attenuation in the mantle beneath north america: Journal of Geophysical Research: Solid Earth, **114**.

Jerkins, A. E., H. A. Shiddiqi, T. Kværna, S. J. Gibbons, J. Schweitzer, L. Ottemöller, and H. Bungum, 2020, The 30 June 2017 North Sea earthquake: location, characteristics, and context: Bulletin of the Seismological Society of America, **110**, 937–952.

Kalkan, E., 2016, An automatic P-phase arrival-time picker: Bulletin of the Seismological Society of America, **106**, 971–986.

Kang, I. B., and G. A. McMechan, 1994, Separation of intrinsic and scattering Q based on frequency-dependent amplitude ratios of transmitted waves: Journal of Geophysical Research: Solid Earth, **99**, 23875–23885.

Keers, H., F. Dahlen, and G. Nolet, 1997, Chaotic ray behaviour in regional seismology: Geophysical Journal International, **131**, 361–380.

Landrø, M., 2002, Uncertainties in quantitative time-lapse seismic analysis: Geophysical prospecting, **50**, 527–538.

Lindsey, N. J., E. R. Martin, D. S. Dreger, B. Freifeld, S. Cole, S. R. James, B. L. Biondi, and J. B. Ajo-Franklin, 2017, Fiber-optic network observations of earthquake wavefields: Geophysical Research Letters, **44**, 11–792.

Liu, N., B. Zhang, J. Gao, Z. Gao, and S. Li, 2018, Seismic attenuation estimation

using the modified log spectral ratio method: Journal of Applied Geophysics, **159**, 386–394.

Malme, T. N., M. Landrø, and R. Mittet, 2005, Overburden distortions—implications for seismic avo analysis and time-lapse seismic: Journal of Geophysics and Engineering, **2**, 81–89.

Mayeda, K., L. Malagnini, and W. R. Walter, 2007, A new spectral ratio method using narrow band coda envelopes: Evidence for non-self-similarity in the Hector Mine sequence: Geophysical Research Letters, **34**.

Mitchell, B. J., 1995, Anelastic structure and evolution of the continental crust and upper mantle from seismic surface wave attenuation: Reviews of Geophysics, **33**, 441–462.

Mitchell, B. J., L. Cong, and G. Ekström, 2008, A continent-wide map of 1-hz Lg coda Q variation across Eurasia and its relation to lithospheric evolution: Journal of Geophysical Research: Solid Earth, **113**.

NORSAR, 1971, NORSAR seismic bulletins.

Reid, F. J., P. H. Nguyen, C. MacBeth, and R. A. Clark, 2001, Q estimates from North sea VSPs, *in* SEG Technical Program Expanded Abstracts 2001: Society of Exploration Geophysicists, 440–443.

Romanowicz, B., and B. Mitchell, 2007, Deep Earth structure Q of the earth from crust to core: Treatise on geophysics, 731–774.

Sams, M., J. Neep, M. Worthington, and M. King, 1997, The measurement of velocity dispersion and frequency-dependent intrinsic attenuation in sedimentary rocks: Geophysics, **62**, 1456–1464.

Schonewille, M., A. Vigner, and A. Ryder, 2008, Swell-noise attenuation using an iterative FX prediction filtering approach, *in* SEG Technical Program Expanded Abstracts 2008: Society of Exploration Geophysicists, 2647–2651.

Sheriff, R. E., and L. P. Geldart, 1995, Exploration seismology: Cambridge university press.

Sketsiou, P., L. De Siena, S. Gabrielli, and F. Napolitano, 2021, 3-D attenuation image of fluid storage and tectonic interactions across the Pollino fault network: Geophysical Journal International, **226**, 536–547.

Solomon, S. C., 1973, Shear wave attenuation and melting beneath the mid-atlantic ridge: Journal of Geophysical Research, **78**, 6044–6059.

Stainsby, S., and M. Worthington, 1985, Q estimation from vertical seismic profile data and anomalous variations in the central North Sea: Geophysics, **50**, 615–626.

Stein, S., and M. Wysession, 2003, An introduction to seismology, earthquakes, and earth structure: Blackwell, Oxford.

Teng, T.-L., 1968, Attenuation of body waves and the q structure of the mantle: Journal of Geophysical Research, **73**, 2195–2208.

Thomson, C., and C. Chapman, 1985, An introduction to Maslov's asymptotic method: Geophysical Journal International, **83**, 143–168.

Tonn, R., 1991, The determination of the seismic quality factor Q from VSP data: a comparison of different computational methods: Geophysical Prospecting, **39**, 1–27.

USGS, 2022, Search earthquake catalog. (Accessed: 2022-06-22).

White, R., 1992, The accuracy of estimating Q from seismic data: Geophysics, **57**,

1508–1511.

Williams, E. F., M. R. Fernández-Ruiz, R. Magalhaes, R. Vanthillo, Z. Zhan, M. González-Herráez, and H. F. Martins, 2019, Distributed sensing of microseisms and teleseisms with submarine dark fibers: Nature communications, **10**, 1–11.

Zollo, A., and S. de Lorenzo, 2001, Source parameters and three-dimensional attenuation structure from the inversion of microearthquake pulse width data: Method and synthetic tests: Journal of Geophysical Research: Solid Earth, **106**, 16287–16306.

LIST OF TABLES

LIST OF FIGURES

time signals on the vertical and (E-W)-geophone components recorded by node 40 on Oseberg PRM. The boxes indicate the time-window used to compute the noise, P- and S-waves amplitude spectra (and later RMS). (C-D) The respective amplitude spectra normalized to the individual maxima for BER and OSE. The noise is black, P-wave red, and S-wave blue. Solid lines represent BER and dashed OSE. (E-F) The time signals recorded on the BER seismometer. The boxes indicate the time-window (of equal size as in (A-B)) used to compute the noise, P- and S-waves amplitude spectra.

5   RMS and SNR for the three earthquakes. (A) E1 computed RMS values for the noise recorded on the vertical (black) and x-component (grey), the P-waves on the vertical component (red) and S-waves on the x-component (blue). (B) The corresponding SNR for the P- and S-wave. The threshold for acceptable P-wave SNR (red dashed lines) is set to 7.5 dB. (C-F) RMS and SNR for E2 and E3.

6   Computation of slopes from E2 using node 90 for smoothed (A-B, D-E, G-H) and unsmoothed (C, F, I) representations of the amplitude spectra. (A-B) The smoothed amplitude spectrum for the P- and S-wave phases recorded on the Oseberg PRM data. (C) The unsmoothed amplitude spectrum for the S-wave phase for OSE. (D-E) The smoothed amplitude spectrum for the P- and S-wave for BER. (F) The unsmoothed amplitude spectrum for the S-wave phase for BER. BER exhibits a higher frequency content than Oseberg, which can be attributed to the extra attenuation in the sediment. (G-H) The computation of the slope (black dashed line) using the frequency components (bold blue segments) with SNR above 10 dB (orange dashed line) is used in the Q_{sed} estimation. For more examples of slope estimates see

Figures S2 to S7 in supplementary materials. (I) The computation of the slope using unsmoothed OSE and BER.

7   (A) Estimated slopes from the P- and S-waves with a 95% confidence interval for E1, E2 and E3. (B) The standard residual error (SRE) of the slope estimates. (C) Estimated Q_p and Q_s values with uncertainty computed using equation 17.

8   Travel times and Δt^* values based on the ray tracing from the earthquakes to OSE used in the Q estimation. (A) The travel times for P-waves through the sediment layer for E2 and E3. (B) Differences in t^* for the P-wave through the layered bedrock model, E1. (C,E) The travel time for the S-wave through the sediment layers for E1 (C), E2 and E3 (E). (D,F) Differences in t^* for the S-wave through the layered bedrock model for E1 (D), E2 and E3 (F).

9   Spatial distribution of the Q_{sed} values along the array. Estimates for S-waves are given in (A) for E1, (C) for E2, and (D) for E3, whereas the estimates for P-waves are given in (B). Gray dots indicate receivers with SNR below 7.5 dB.

10   Raw Q estimation. The accepted (blue) and rejected (red) Q_p (A) and Q_s (B) estimates. Note that the Q_p values for E1 are rejected due to high noise contamination for all channels (see Figure 5), whereas Q_p for E2 and E3 are rejected based on a combination of high noise level and high errors in the regression analysis.

11   The total uncertainty in the estimated average quality factor obtained from P-waves, E2. (A) Uncertainty as a function of slope values. (B) Uncertainty as a function of travel times through the sedimentary sequence. (C) Uncertainty as a function of Δt^* values (see equation 12). For each plot, the range is taken as $\pm 75\%$ of the average values obtained from the analysis (black crosses). The dashed lines are

40

associated with an -15% error in the velocity model, whereas the solid line an $+15\%$ error.

12 The total uncertainty in the estimated average quality factor obtained from S-waves, E2. (A) Uncertainty as a function of slope values. (B) Uncertainty as a function of travel times through the sedimentary sequence. (C) Uncertainty as a function of Δt^* values (see equation 12). For each plot, the range is taken as $\pm 75\%$ of the average values obtained from the analysis (black crosses). The dashed lines are associated with an -15% error in the velocity model, whereas the solid line an $+15\%$ error.

B-1 Example of high and low SNR waveforms at Oseberg. (A-B) Hydrophone component with a clear P-wave onset. (C-D) Geophone (E-W)-component, clear S-arrival. (E-F) Geophone (N-S)-component, clear S-arrival. (G-H) Geophone vertical component is clear P-arrival in (G) and unclear in (H). Panels (A,C,E,G) show the recordings on node 90, while (B,D,F,H) show node 60.

C-1 Notches observed on node 30 in the PRM system compared to predicted interference patter for a water depth of $\simeq 107$ m. (A) The predicted interference pattern (yellow dashed line) matches the observed P-wave train amplitude spectrum recorded by geophone at Oseberg. The black line shows the original amplitude spectrum, while the red shows the smoothed version. (B) Shows how the predicted interference partly fit the observed S-wave train amplitude spectrum, not as good as for the P-wave. Most likely because the S-wave do not propagate in liquids, and an S-P conversion is needed to create the notches. (C) The predicted interference pattern for the hydrophone correlates well with the observed amplitude spectrum.

42

42

Figure 1: Overview of the region of interest. (A) The study area relative to Europe, the red rectangle shows the study area (bathymetry map from GEBCO (2021)). (B) The location of the earthquakes (orange starts) with associated error ellipses and the receivers (red triangles). (C) The receiver geometry of the 172 OBN just south of the Oseberg C platform.

Table 1: Information for the local earthquakes used to estimate the quality factors.

Figure 2: Suppression of platform noise from Oseberg C. (A) The raw observed signals. (B) The observed signal after the fx-filter. (C) The difference between (A) and (B). This shows that the noise closest to the platform (channels 1-16, 80-100, 157-172) has successfully been suppressed. The dashed rectangle indicates the area used for the analysis, the nodes closest to the platform (1-14 and 159-172) is too contaminated by platform noise to give reliable results and are discarded a priori to the analysis.

Figure 3: Velocity model and conceptual sketch. (A) The sonic log from well 30/6-1 (blue) and the smoothed version (red) with the assumed 15% uncertainty indicated (red dashed lines). (B) The final velocity model (red), combining the smoothed sonic log and Norwegian National Seismic Network's (NNSN) P-wave crustal velocity model (blue). (C) The ray paths to BER is assumed to be dominated by attenuation in bedrock, while the travel path to Oseberg is affected by attenuation from a 5-7 km thick sediment package and the same bedrock model as for the ray path to BER. The Q-model of the bedrock is assumed known, while the value (Q_{sed}) for the sediment package is estimated.

Table 2: The mean value, with one standard deviation, for the different terms in equation 11 using a three-layered bedrock quality factor (Q) model (see Figure 3 for Q-model). The mean and standard deviation are found from the different values obtained as described in the Data and Theory section. The quantified uncertainties are presented later.

Figure 4: The time- and frequency content of the different recording sites. (A-B) The time signals on the vertical and (E-W)-geophone components recorded by node 40 on Oseberg PRM. The boxes indicate the time-window used to compute the noise, P- and S-waves amplitude spectra (and later RMS). (C-D) The respective amplitude spectra normalized to the individual maxima for BER and OSE. The noise is black, P-wave red, and S-wave blue. Solid lines represent BER and dashed OSE. (E-F) The time signals recorded on the BER seismometer. The boxes indicate the time-window (of equal size as in (A-B)) used to compute the noise, P- and S-waves amplitude spectra.

Figure 5: RMS and SNR for the three earthquakes. (A) E1 computed RMS values for the noise recorded on the vertical (black) and x-component (grey), the P-waves on the vertical component (red) and S-waves on the x-component (blue). (B) The corresponding SNR for the P- and S-wave. The threshold for acceptable P-wave SNR (red dashed lines) is set to 7.5 dB. (C-F) RMS and SNR for E2 and E3.

Figure 6: Computation of slopes from E2 using node 90 for smoothed (A-B, D-E, G-H) and unsmoothed (C, F, I) representations of the amplitude spectra. (A-B) The smoothed amplitude spectrum for the P- and S-wave phases recorded on the Oseberg PRM data. (C) The unsmoothed amplitude spectrum for the S-wave phase for OSE. (D-E) The smoothed amplitude spectrum for the P- and S-wave for BER. (F) The unsmoothed amplitude spectrum for the S-wave phase for BER. BER exhibits a higher frequency content than Oseberg, which can be attributed to the extra attenuation in the sediment. (G-H) The computation of the slope (black dashed line) using the frequency components (bold blue segments) with SNR above 10 dB (orange dashed line) is used in the Q_{sed} estimation. For more examples of slope estimates see Figures S2 to S7 in supplementary materials. (I) The computation of the slope using unsmoothed OSE and BER.

Figure 7: (A) Estimated slopes from the P- and S-waves with a 95% confidence interval for E1, E2 and E3. (B) The standard residual error (SRE) of the slope estimates. (C) Estimated Q_p and Q_s values with uncertainty computed using equation 17.

52

Figure 8: Travel times and Δt^* values based on the ray tracing from the earthquakes to OSE used in the Q estimation. (A) The travel times for P-waves through the sediment layer for E2 and E3. (B) Differences in t^* for the P-wave through the layered bedrock model, E1. (C,E) The travel time for the S-wave through the sediment layers for E1 (C), E2 and E3 (E). (D,F) Differences in t^* for the S-wave through the layered bedrock model for E1 (D), E2 and E3 (F).

Figure 9: Spatial distribution of the Q_{sed} values along the array. Estimates for S-waves are given in (A) for E1, (C) for E2, and (D) for E3, whereas the estimates for P-waves are given in (B). Gray dots indicate receivers with SNR below 7.5 dB.

Figure 10: Raw Q estimation. The accepted (blue) and rejected (red) Q_p (A) and Q_s (B) estimates. Note that the Q_p values for E1 are rejected due to high noise contamination for all channels (see Figure 5), whereas Q_p for E2 and E3 are rejected based on a combination of high noise level and high errors in the regression analysis.

55

Table 3: Q_{sed} estimation results are given as the mean, with one standard deviation (Q_p for E3 has one value), of all stations adhering to the first SNR condition. The Q_s/Q_p values are taken for central channels with estimations for both wave types. N denotes the number of data points for the different estimates.

Figure 11: The total uncertainty in the estimated average quality factor obtained from P-waves, E2. (A) Uncertainty as a function of slope values. (B) Uncertainty as a function of travel times through the sedimentary sequence. (C) Uncertainty as a function of Δt^* values (see equation 12). For each plot, the range is taken as $\pm 75\%$ of the average values obtained from the analysis (black crosses). The dashed lines are associated with an -15% error in the velocity model, whereas the solid line an $+15\%$ error.

Figure 12: The total uncertainty in the estimated average quality factor obtained from S-waves, E2. (A) Uncertainty as a function of slope values. (B) Uncertainty as a function of travel times through the sedimentary sequence. (C) Uncertainty as a function of Δt^* values (see equation 12). For each plot, the range is taken as $\pm 75\%$ of the average values obtained from the analysis (black crosses). The dashed lines are associated with an -15% error in the velocity model, whereas the solid line an $+15\%$ error.

Figure B-1: Example of high and low SNR waveforms at Oseberg. (A-B) Hydrophone component with a clear P-wave onset. (C-D) Geophone (E-W)-component, clear S-arrival. (E-F) Geophone (N-S)-component, clear S-arrival. (G-H) Geophone vertical component is clear P-arrival in (G) and unclear in (H). Panels (A,C,E,G) show the recordings on node 90, while (B,D,F,H) show node 60.

Figure C-1: Notches observed on node 30 in the PRM system compared to predicted interference patter for a water depth of $\simeq 107$ m. (A) The predicted interference pattern (yellow dashed line) matches the observed P-wave train amplitude spectrum recorded by geophone at Oseberg. The black line shows the original amplitude spectrum, while the red shows the smoothed version. (B) Shows how the predicted interference partly fit the observed S-wave train amplitude spectrum, not as good as for the P-wave. Most likely because the S-wave do not propagate in liquids, and an S-P conversion is needed to create the notches. (C) The predicted interference pattern for the hydrophone correlates well with the observed amplitude spectrum.

Figure_1_A-C: Overview of the region of interest. (A) The study area relative to Europe, the red rectangle shows the study area (bathymetry map from GEBCO (2021)). (B) The location of the earthquakes (orange starts) with associated error ellipses and the receivers (red triangles). (C) The receiver geometry of the 172 OBN just south of the Oseberg C platform.

647x512mm (177 x 177 DPI)
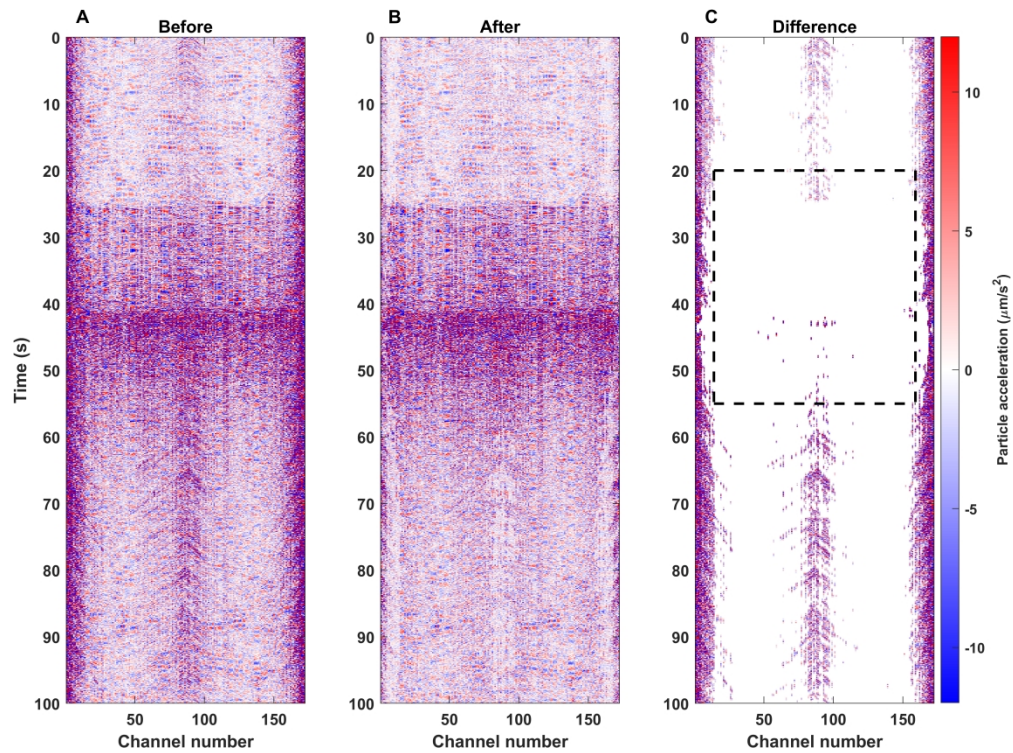
Figure_2_A-C: Suppression of platform noise from Oseberg C. (A) The raw observed signals. (B) The observed signal after the fx-filter. (C) The difference between (A) and (B). This shows that the noise closest to the platform (channels 1-16, 80-100, 157-172) has successfully been suppressed. The dashed rectangle indicates the area used for the analysis, the nodes closest to the platform (1-14 and 159-172) is too contaminated by platform noise to give reliable results and are discarded a priori to the analysis.

684x506mm (177 x 177 DPI)
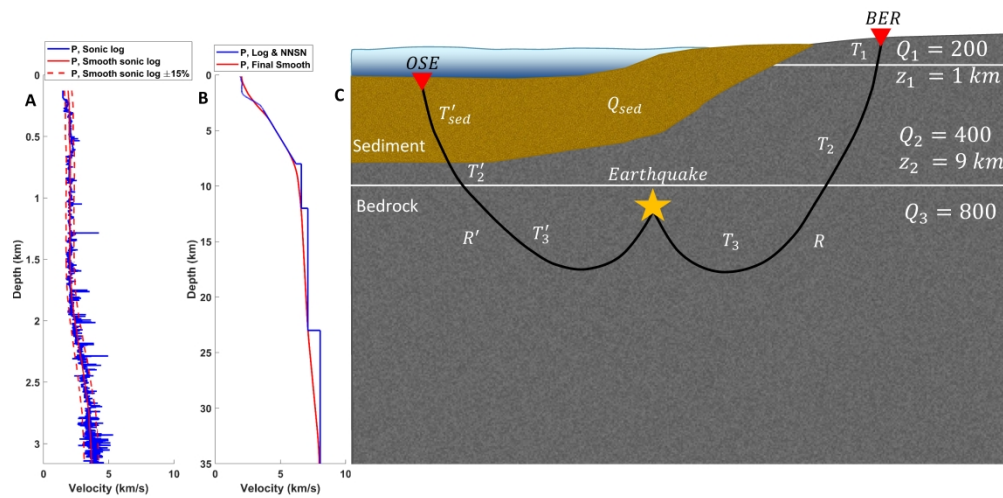
Figure_3_A-C: Velocity model and conceptual sketch. (A) The sonic log from well 30/6-1 (blue) and the smoothed version (red) with the assumed 15% uncertainty indicated (red dashed lines). (B) The final velocity model (red), combining the smoothed sonic log and Norwegian National Seismic Network's (NNSN) P-wave crustal velocity model (blue). (C) The ray paths to BER is assumed to be dominated by attenuation in bedrock, while the travel path to Oseberg is affected by attenuation from a 5-7 km thick sediment package and the same bedrock model as for the ray path to BER. The Q-model of the bedrock is assumed known, while the value (Qsed) for the sediment package is estimated.

860x421mm (236 x 236 DPI)
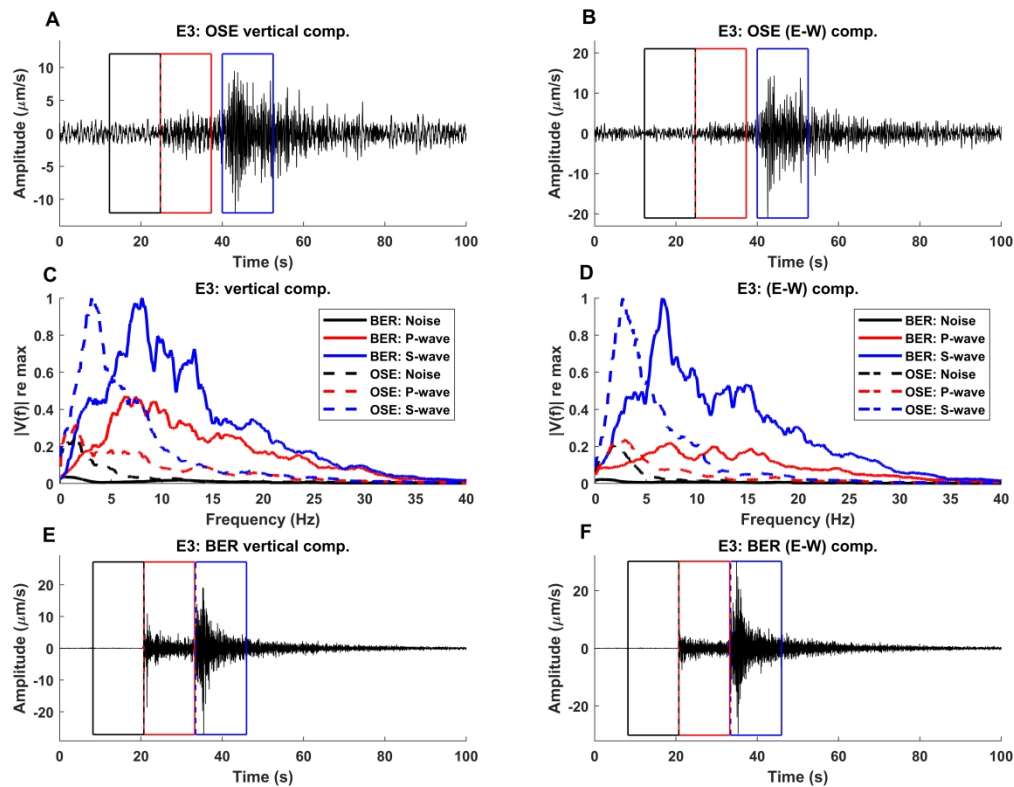
Figure_4_A-F: The time- and frequency content of the different recording sites. (A-B) The time signals on the vertical and (E-W)-geophone components recorded by node 40 on Oseberg PRM. The boxes indicate the time-window used to compute the noise, P- and S-waves amplitude spectra (and later RMS). (C-D) The respective amplitude spectra normalized to the individual maxima for BER and OSE. The noise is black, P-wave red, and S-wave blue. Solid lines represent BER and dashed OSE. (E-F) The time signals recorded on the BER seismometer. The boxes indicate the time-window (of equal size as in (A-B)) used to compute the noise, P- and S-waves amplitude spectra.

621x482mm (236 x 236 DPI)
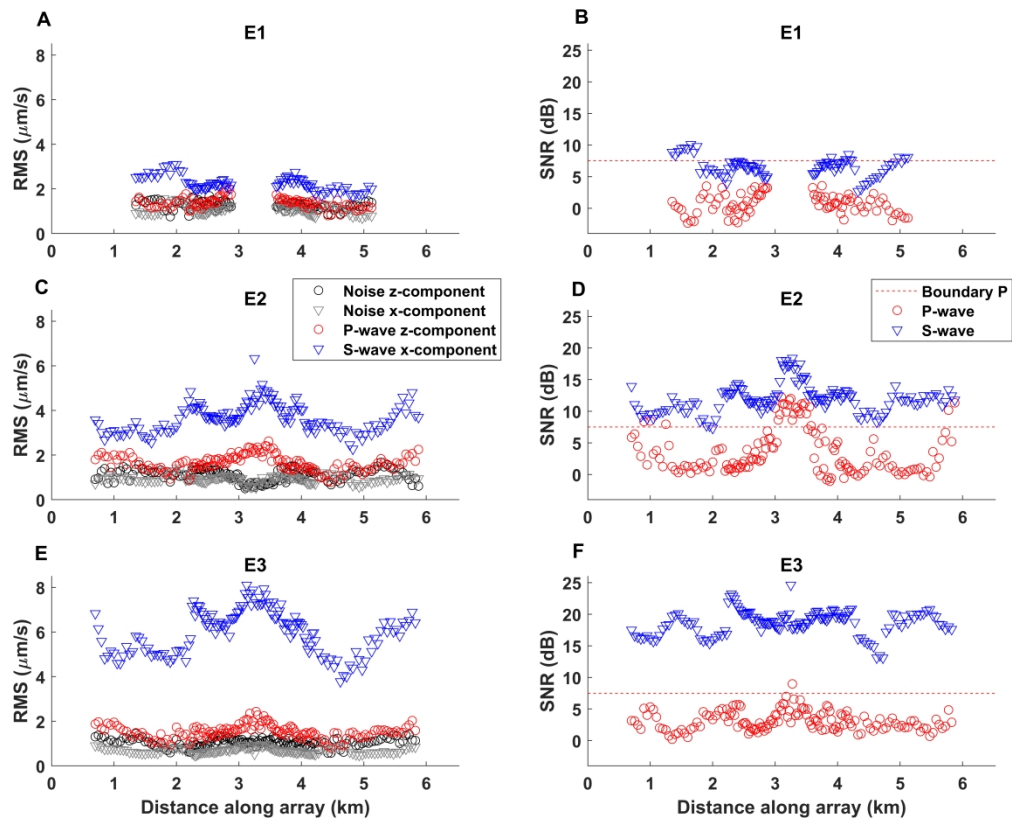
Figure_5_A-F: RMS and SNR for the three earthquakes. (A) E1 computed RMS values for the noise recorded on the vertical (black) and x-component (grey), the P-waves on the vertical component (red) and S-waves on the x-component (blue). (B) The corresponding SNR for the P- and S-wave. The threshold for acceptable P-wave SNR (red dashed lines) is set to 7.5 dB. (C-F) RMS and SNR for E2 and E3

630x509mm (236 x 236 DPI)
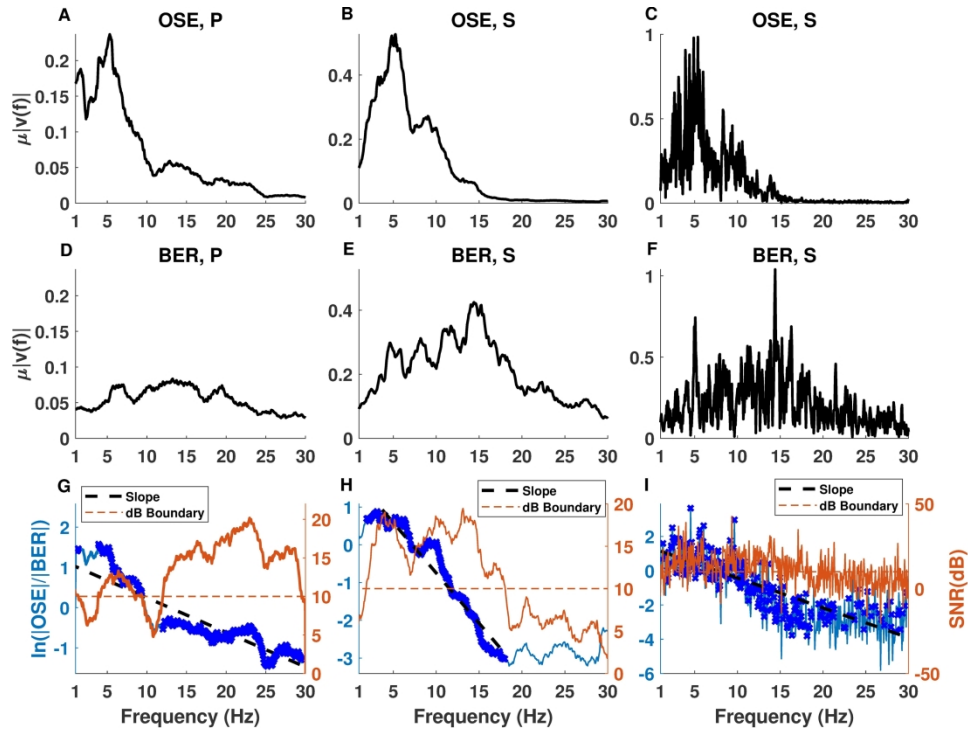
Figure_6_A-I_v: Computation of slopes from E2 using node 90 for smoothed (A-B, D-E, G-H) and unsmoothed (C, F, I) representations of the amplitude spectra. (A-B) The smoothed amplitude spectrum for the P- and S-wave phases recorded on the Oseberg PRM data. (C) The unsmoothed amplitude spectrum for the S-wave phase for OSE. (D-E) The smoothed amplitude spectrum for the P- and S-wave for BER. (F) The unsmoothed amplitude spectrum for the S-wave phase for BER. BER exhibits a higher frequency content than Oseberg, which can be attributed to the extra attenuation in the sediment. (G-H) The computation of the slope (black dashed line) using the frequency components (bold blue segments) with SNR above 10 dB (orange dashed line) is used in the Qsed estimation. For more examples of slope estimates see Figures S2 to S7 in supplementary materials. (I) The computation of the slope using unsmoothed OSE and BER.

280x202mm (300 x 300 DPI)
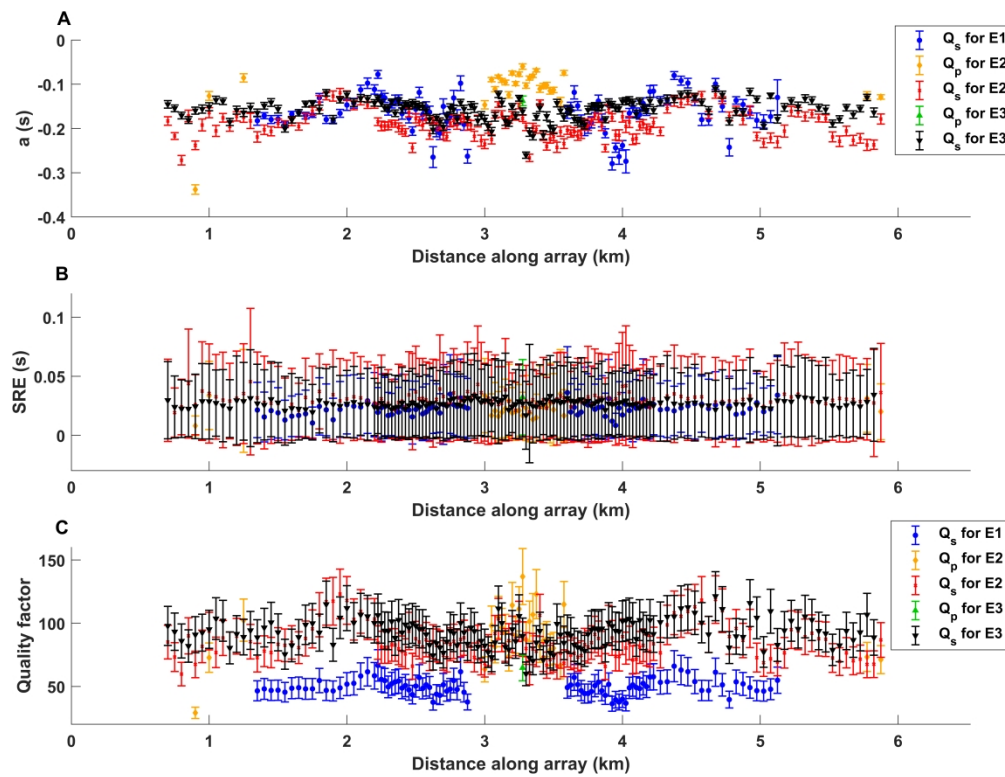
Figure_7_A-C: (A) Estimated slopes from the P- and S-waves with a 95% confidence interval for E1, E2 and E3. (B) The standard residual error (SRE) of the slope estimates. (C) Estimated Qp and Qs values with uncertainty computed using equation 17.

661x504mm (236 x 236 DPI)
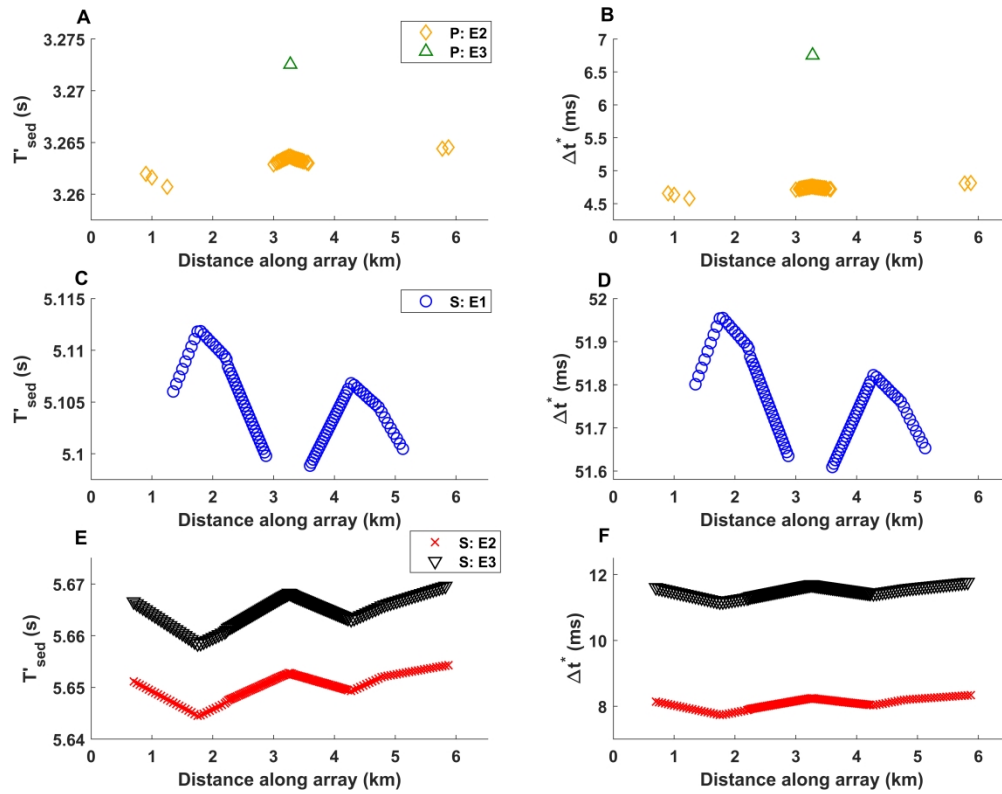
Figure_8_A-F: Travel times and δt* values based on the ray tracing from the earthquakes to OSE used in the Q estimation. (A) The travel times for P-waves through the sediment layer for E2 and E3. (B) Differences in t* for the P-wave through the layered bedrock model, E1. (C,E) The travel time for the S-wave through the sediment layers for E1 (C), E2 and E3 (E). (D,F) Differences in t* for the S-wave through the layered bedrock model for E1 (D), E2 and E3 (F).

646x505mm (236 x 236 DPI)
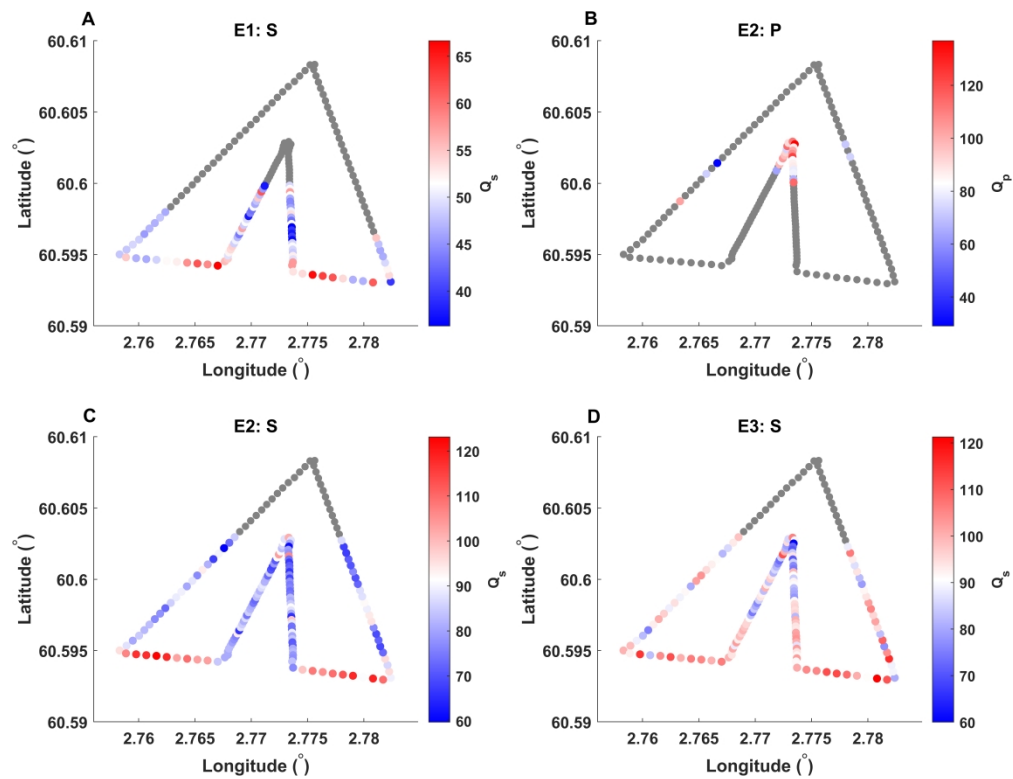
Figure_9_A-D: Spatial distribution of the Qsed values along the array. Estimates for S-waves are given in (A) for E1, (C) for E2, and (D) for E3, whereas the estimates for P-waves are given in (B). Gray dots indicate receivers with SNR below 7.5 dB.

670x512mm (236 x 236 DPI)
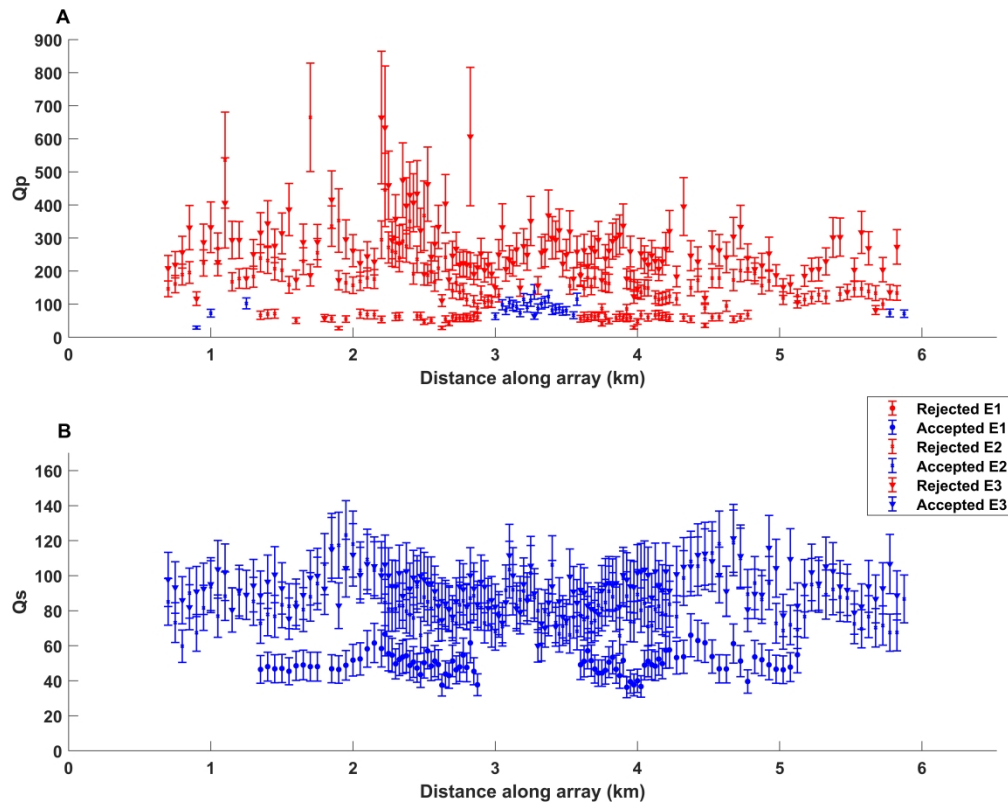
Figure_10_A-B: Raw Q estimation. The accepted (blue) and rejected (red) Qp (A) and Qs (B) estimates. Note that the Qp values for E1 are rejected due to high noise contamination for all channels (see Figure 5), whereas Qp for E2 and E3 are rejected based on a combination of high noise level and high errors in the regression analysis.

641x508mm (236 x 236 DPI)
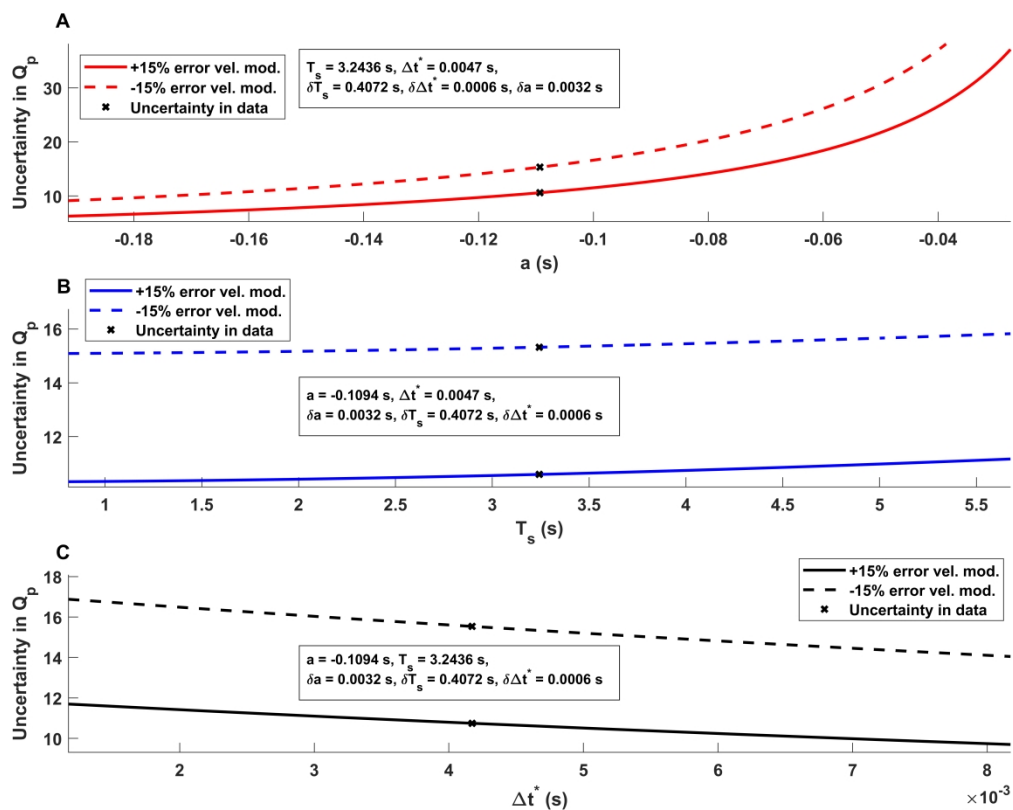
Figure_11_A-C: The total uncertainty in the estimated average quality factor obtained from P-waves, E2. (A) Uncertainty as a function of slope values. (B) Uncertainty as a function of travel times through the sedimentary sequence. (C) Uncertainty as a function of δt* values (see equation 12). For each plot, the range is taken as ±75% of the average values obtained from the analysis (black crosses). The dashed lines are associated with an -15% error in the velocity model, whereas the solid line an +15% error.

631x503mm (236 x 236 DPI)
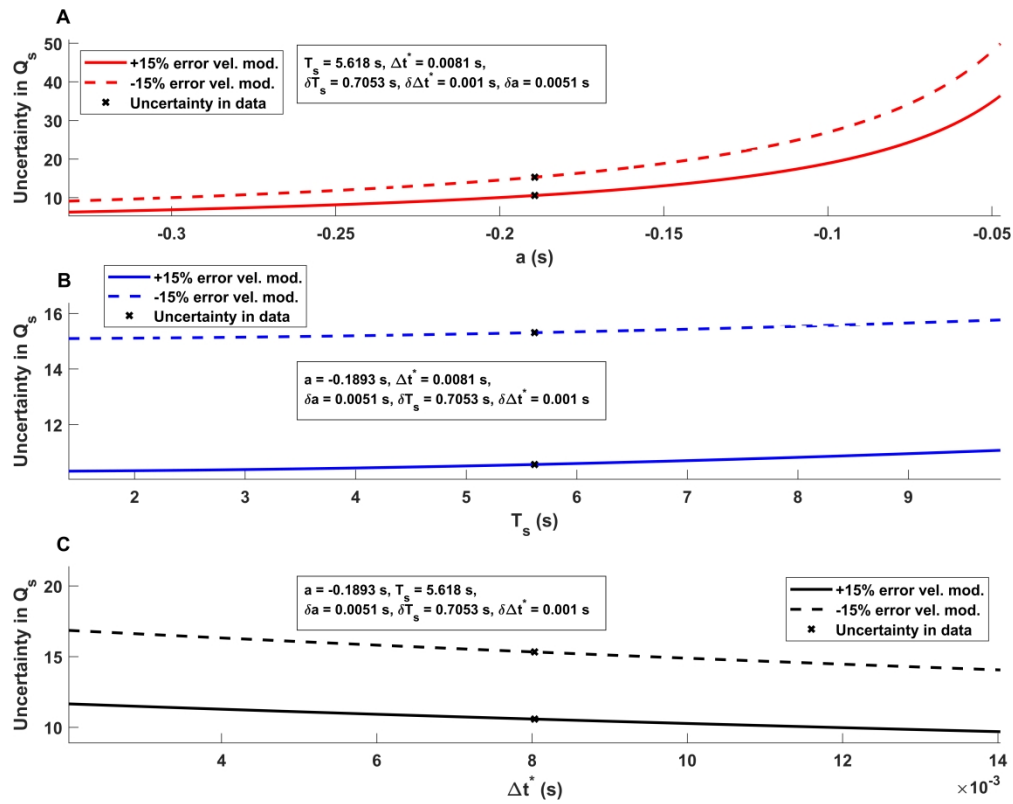
Figure_12_A-C: The total uncertainty in the estimated average quality factor obtained from S-waves, E2. (A) Uncertainty as a function of slope values. (B) Uncertainty as a function of travel times through the sedimentary sequence. (C) Uncertainty as a function of δt* values (see equation 12). For each plot, the range is taken as ±75% of the average values obtained from the analysis (black crosses). The dashed lines are associated with an -15% error in the velocity model, whereas the solid line an +15% error.

637x503mm (236 x 236 DPI)
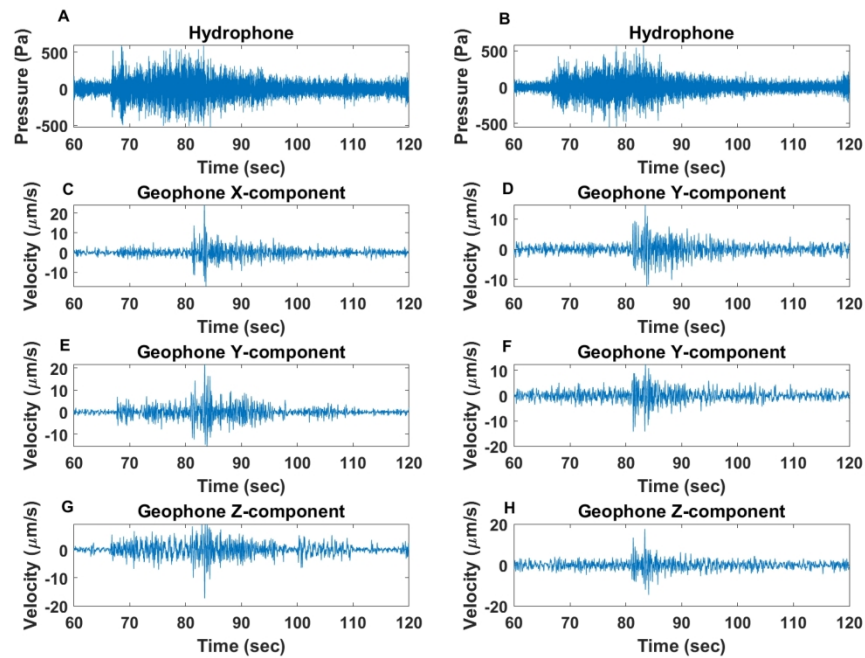
Figure_B-1_A-H_v: Example of high and low SNR waveforms at Oseberg. (A-B) Hydrophone component with a clear P-wave onset. (C-D) Geophone (E-W)-component, clear S-arrival. (E-F) Geophone (N-S)-component, clear S-arrival. (G-H) Geophone vertical component is clear P-arrival in (G) and unclear in (H). Panels (A,C,E,G) show the recordings on node 90, while (B,D,F,H) show node 60.

301x220mm (300 x 300 DPI)
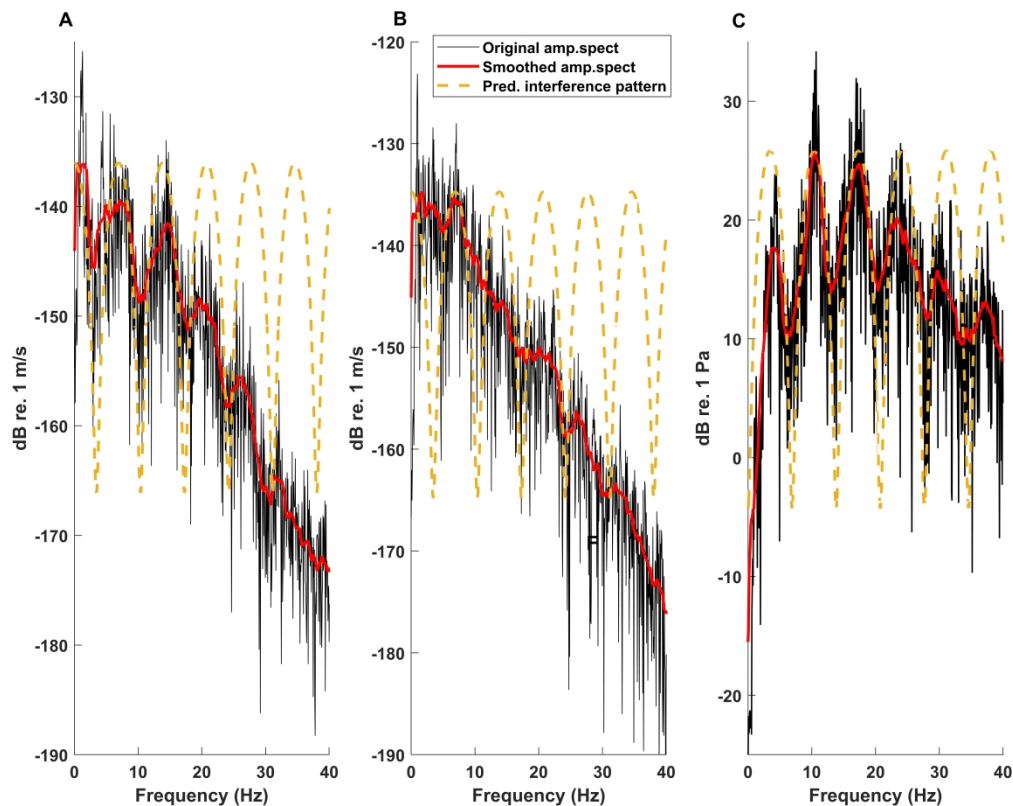
Figure_C-1_A-C: Notches observed on node 30 in the PRM system compared to predicted interference pattern for a water depth of 107 m. (A) The predicted interference pattern (yellow dashed line) matches the observed P-wave train amplitude spectrum recorded by geophone at Oseberg. The black line shows the original amplitude spectrum, while the red shows the smoothed version. (B) Shows how the predicted interference partly fit the observed S-wave train amplitude spectrum, not as good as for the P-wave. Most likely because the S-wave do not propagate in liquids, and an S-P conversion is needed to create the notches. (C) The predicted interference pattern for the hydrophone correlates well with the observed amplitude spectrum.

640x508mm (236 x 236 DPI)

LIST OF TABLES

1

Name	Date	Time	(Lat°, Lon°)	Depth (km)	Magnitude (M_L)	Station	Distance (km)
E1	2014.01.16	17:03:31	(59.51°, 1.47°)	-	2.11	BER	239
						OSE	142
E2	2014.01.21	06:39:04	(61.05°, 4.72°)	13.6	2.35	BER	107
						OSE	88
E3	2014.01.23	04:32:50	(61.24°, 4.70°)	9.6	2.57	BER	119
						OSE	107

Table 1

2

LIST OF TABLES

1

Name	Wave	$-a/\pi$ (s)	Δt^* (s)	$T_1 - T_2$ (s)	T'_{sed} (s)
E1	S	0.052 ± 0.01	0.052	-34.7 ± 0.08	5.10 ± 0.0006
E2	P	0.035 ± 0.02	0.005	0.84 ± 0.08	3.27 ± 0.002
E2	S	0.060 ± 0.01	0.008	1.46 ± 0.13	5.65 ± 0.003
E3	P	0.044	0.007	-0.84	3.27
E3	S	0.050 ± 0.008	0.012	-1.35 ± 0.14	5.67 ± 0.003

Table 1

LIST OF TABLES

Name	N_p	Q_p	N_s	Q_s	$N_{Qs/Qp}$	Q_s/Q_p
E1	0	-	89	50 ± 6	0	-
E2	26	92 ± 18	145	84 ± 13	22	0.9 ± 0.2
E3	1	65	144	93 ± 13	1	1.4

Table 1: .

2